Fitting peculiar spectral profiles in He I 10830 Å absorption features

S. J. González Manrique[1,2,⋆], **C. Kuckein**[1], **A. Pastor Yabar**[3,4], **M. Collados**[3], **C. Denker**[1], **C.E. Fischer**[5], **P. Gömöry**[6,1], **A. Diercke**[1,2], **N. Bello González**[5], **R. Schlichenmaier**[5], **H. Balthasar**[1], **T. Berkefeld**[5], **A. Feller**[8], **S. Hoch**[5], **A. Hofmann**[1], **F. Kneer**[9], **A. Lagg**[8], **H. Nicklas**[9], **D. Orozco Suárez**[3,4], **D. Schmidt**[10], **W. Schmidt**[5], **M. Sigwarth**[5], **M. Sobotka**[7], **S.K. Solanki**[8,11], **D. Soltau**[5], **J. Staude**[1], **K.G. Strassmeier**[1], **M. Verma**[1], **R. Volkmer**[5], **O. von der Lühe**[5], and **T. Waldmann**[5]

[1] Leibniz-Institut für Astrophysik Potsdam (AIP), An der Sternwarte 16, 14482 Potsdam, Germany
[2] Universität Potsdam, Institut für Physik and Astronomie, Karl-Liebknecht-Straße 24/25, 14476 Potsdam-Golm, Germany
[3] Instituto de Astrofísica de Canarias, c/ Vía Láctea s/n, La Laguna 38205, Spain
[4] Dept. Astrofsica, Universidad de La Laguna, E-38205, La Laguna, Tenerife, Spain
[5] Kiepenheuer-Institut für Sonnenphysik, Schöneckstr. 6, 79104 Freiburg, Germany
[6] Astronomical Institute of the Slovak Academy of Sciences, 05960 Tatranská Lomnica, Slovakia
[7] Astronomical Institute, Academy of Sciences of the Czech Republic, Fričova 298, 25165 Ondřejov, Czech Republic
[8] Max-Planck-Institut für Sonnensystemforschung, Justus-von-Liebig-Weg 3, 37077 Göttingen, Germany
[9] Institut für Astrophysik, Georg-August-Universität Göttingen, Friedrich-Hund-Platz 1, 37077 Göttingen, Germany
[10] National Solar Observatory, 3010 Coronal Loop Sunspot, NM 88349, USA
[11] School of Space Research, Kyung Hee University, Yongin, Gyeonggi-Do, 446-701, Korea

The new generation of solar instruments provides better spectral, spatial, and temporal resolution for a better understanding of the physical processes that take place on the Sun. Multiple-component profiles are more commonly observed with these instruments. Particularly, the He I 10830 Å triplet presents such peculiar spectral profiles, which give information on the velocity and magnetic fine structure of the upper chromosphere. The purpose of this investigation is to describe a technique to efficiently fit the two blended components of the He I 10830 Å triplet, which are commonly observed when two atmospheric components are located within the same resolution element. The observations used in this study were taken on 2015 April 17 with the very fast spectroscopic mode of the GREGOR Infrared Spectrograph (GRIS) attached to the 1.5-m GREGOR solar telescope, located at the Observatorio del Teide, Tenerife, Spain. We apply a double-Lorentzian fitting technique using Levenberg-Marquardt least-squares minimization. This technique is very simple and much faster than inversion codes. Line-of-sight Doppler velocities can be inferred for a whole map of pixels within just a few minutes. Our results show sub- and supersonic downflow velocities of up to $32\,\mathrm{km\,s^{-1}}$ for the fast component in the vicinity of footpoints of filamentary structures. The slow component presents velocities close to rest.

© 2016 WILEY-VCH Verlag GmbH & Co. KGaA, Weinheim

1 Introduction

The spectral window around the He I 10830 Å triplet has often been used to study the magnetic properties and dynamics in the solar chromosphere. The height of formation of this triplet lies in the upper chromosphere (Avrett et al. 1994). It comprises three transitions, which take place between the lower 2^3S_1 level and the upper $2^3P_{2,1,0}$ level. However, two transitions are blended and therefore only two spectral lines are observed. Generally, the blended line at ~ 10830.30 Å is called "red" component, while the non-blended line at 10829.09 Å is called the "blue" component. The wavelengths were taken from the National Institute of Standards and Technology (NIST).[1]

Of special interest are the strongly redshifted He I profiles, which have been reported by several authors (e.g., Muglach et al. 1997; Muglach & Sütterlin 1998; Penn & Kuhn 1995). Commonly observed are two atmospheric components located within the same resolution element (Lagg et al. 2007). These "dual flows" were reported for the first time by Schmidt et al. (2000) and have an easily recognizable spectral pattern with two or more peaks next to the red component of He I. One of the peaks is often subsonic while the other reaches supersonic velocities. At the average formation temperature of the He I triplet, velocities close to $10\,\mathrm{km\,s^{-1}}$ correspond to the sound speed (Lagg et al. 2007). From now on we will label the profiles, which clearly show dual flow components of the He I triplet as the slow (the one close to rest) and fast (redshifted with respected to the slow one) components.

⋆ Corresponding author: smanrique@aip.de

[1] http://www.nist.gov/
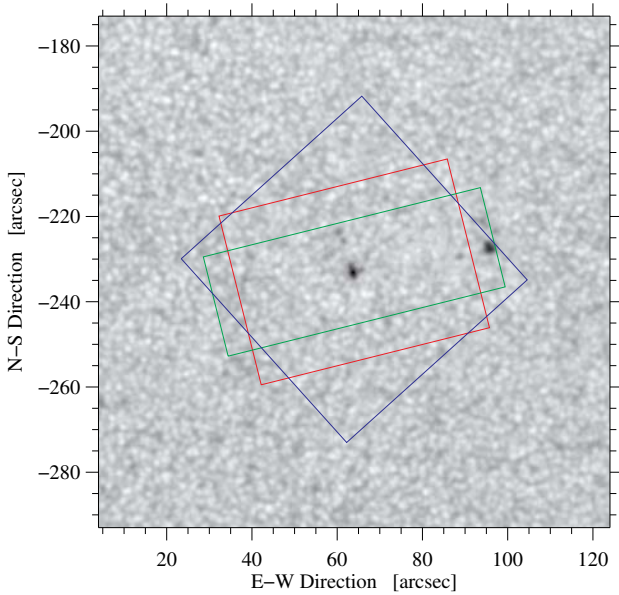
Fig. 1 Overlap of the FOV of the three instruments: GRIS (green), GFPI (red), and CRISP (blue). The background continuum image is from SDO/HMI taken at 08:47 UT on 2015 April 17.

Several studies reported on dual or multiple-peak He I profiles in different phenomena on the Sun, e.g., Teriaca et al. (2003) in two ribbon flares, Sasso et al. (2011, 2007) during a C2.0 flare, Lagg et al. (2007) during an emerging flux process in an active region, or Aznar Cuadrado et al. (2005, 2007) in active and quiet-Sun regions. All of them reported supersonic velocities of the fast component between 40 and 90 km s^{-1}. Lagg et al. (2007) suggested that these dual flows are formed in extremely filamentary structures and that their origin might be related to the magnetic field. It is expected that these profiles provide information on two different heights in the atmosphere.

Several inversion codes are able to synthesize and invert the Stokes profiles of the He I 10830 Å triplet, for example, the He-Line Information Extractor code (HeLIx$^+$, Lagg et al. 2009, 2004), the HAnle and ZEeman Light code (HAZEL, Asensio Ramos et al. 2008), or the Milne-Eddington Line Analysis using a Numerical Inversion Engine (MELANIE, Socas-Navarro 2001). These codes infer the physical parameters such as, e.g., the line-of-sight (LOS) velocity and the vector magnetic field, among others. Usually these inversion codes require considerable computation time. In this paper, we present a simple and very fast technique to infer the LOS velocities for single and double-peaked profiles. Thus, the information present in the polarized Stokes parameters is disregarded. In particular, we adapted the technique to fit the slow and fast components of the He I 10830 Å triplet.

2 Observations

Our two-component fitting code was applied to one data set acquired with the 1.5-m GREGOR solar telescope (Denker et al. 2012; Schmidt et al. 2012) at Observatorio del Teide, Tenerife, Spain. An emerging flux region (EFR) located at heliographic coordinates S19 and W4 ($\mu \equiv \cos\theta = 0.97$) was observed on 2015 April 17 between 08:16 UT and 09:18 UT. Several instruments and telescopes were involved in this campaign. We will concentrate on the GREGOR Infrared Spectrograph (GRIS, Collados et al. 2012).

For the first time the instrument was operated in the very fast spectroscopic mode (no polarimetry) in the He I 10830 Å spectral region. Typically, in polarimetric mode several integrations reduce the noise in the spectra but also prolong the cadence of the scans. The fast mode relies on a single integration and accepts higher noise in exchange for an improved cadence. The standard deviation $\sigma = 3.3\%$ of the normalized quiet-Sun continuum in the wavelength range 10835.8–10837.1 Å for all spectra in the scan gives an estimate of the noise level, which will slightly increase for darker features like pores.

The spectral window of about 18 Å comprised the photospheric Si I 10827 Å line, the chromospheric He I 10830 Å triplet, the photospheric Ca I 10834 and 10839 Å lines, and several telluric lines among other weaker spectral lines. The spectral sampling was $\delta_\lambda = 18.03$ mÅ pix^{-1}, and the number of spectral points was $N_\lambda = 1010$. The slit was by chance in parallel to two small pores belonging to the EFR (see Fig. 1). The pixel size along the slit was $\sim 0.''136$, thus covering a length of 66$.''$3. For each position of the slit, the integration time was $t = 100$ ms with only one accumulation. This allowed for very fast spectroscopic scans covering an height of 24$.''$12 (with 180 steps and a step size of $\sim 0.''134$) in only ~ 58 s. During roughly one hour of observations (62 min), the GREGOR's altitude-azimuthal mount introduced an image rotation, which had to be corrected (Volkmer et al. 2012). The total rotation angle for the period of observation was 22°3. However, the image rotation for each map is small (never larger than 0°4) and therefore negligible.

In total, 65 scans were taken covering an area of 66$.''$3 × 24$.''$12. Nevertheless, only one map (08:42–08:43 UT) with abundant two-component profiles will be presented in this work (see Fig. 2). The data were taken under good seeing conditions with real-time corrections provided by the GREGOR Adaptive Optics System (GAOS, Berkefeld et al. 2012). Simultaneous multi-wavelength observations were carried out with additional instruments including the GREGOR Fabry-Pérot Interferometer (GFPI, Denker et al. 2010; Puschmann et al. 2012) at the GREGOR telescope and the CRisp Imaging Spectro-Polarimeter (CRISP, Scharmer et al. 2008) installed at the Swedish Solar Telescope (SST, Scharmer et al. 2003) located at Observatorio Roque de los Muchachos, La Palma, Spain. An overview of all the involved FOVs is shown in Fig. 1 after alignment with a

continuum image of the Helioseismic and Magnetic Imager (HMI, Scherrer et al. 2012; Schou et al. 2012) on-board the Solar Dynamics Observatory (SDO, Pesnell et al. 2012). The analysis of the full data set and an investigation of the dynamics related to the EFR are deferred to a forthcoming publication.

2.1 Data reduction

Dark and flat-field corrections were applied as part of the data reduction. The proper continuum of the GRIS spectra was derived by comparing the average quiet-Sun spectrum $I_{QS}(\lambda)$ with that of a Fourier Transform Spectrometer (FTS, Neckel & Labs 1984), which was convolved with a Gaussian to take into account the degradation of the observed spectrum by straylight (see Allende Prieto et al. 2004, for a description of the procedure). The average quiet-Sun profile was computed in an area where the He I absorption was almost absent. Common fringes were removed by multiplying every spectrum by the ratio between the equivalent quiet-Sun mean profile and the quiet-Sun mean profile I'/I_{QS}. Dust particles along the slit and other bright artifacts had to be removed from the data by using an additional flat field based on the science data assuming that the granulation was uniform and isotropic. Abnormal intensity peaks were found along some spectra due to the bad pixels on the detector chip. The peaks were detected by calculating the wavelength derivative of the spectrum of each pixel and searching for absolute values above a suitable threshold. Abnormal intensities were then replaced by an interpolated value between the previous and the next pixels.

The wavelength calibration was carried out using the two telluric lines located next to the He I 10830 Å triplet. An area of the quiet Sun was chosen to compute an average intensity profile. A direct comparison between the separation of the two telluric lines of the averaged intensity profile and the atlas profile of the Fourier Transform Spectrometer (Neckel & Labs 1984) provided the dispersion (18.03 mÅ pix^{-1}). The first telluric line at 10832.108 Å was then used as the wavelength reference. In addition, the wavelength scale was corrected for solar orbital motion and rotation, Earth's rotation, and the solar gravitational redshift. (see appendices A and B in Kuckein et al. 2012).

The fast component is blended by a telluric line for high LOS velocities. Therefore, the telluric line was removed from our spectra. To accomplish this task we averaged all spectral profiles from the map to compute a mean intensity profile. We assumed that the telluric line has a constant wavelength, i.e., it does not shift along the wavelength axis at any time. The telluric line was fitted in the spectral range of 10831.48–10832.56 Å with a single Lorentzian profile. Hence, we have computed a synthetic telluric profile. The telluric line was then removed by dividing each spectrum by the synthetic profile. A smooth transition of the spectrum at the location where the telluric line started was assured by forcing the continuum in the line wings of the telluric line
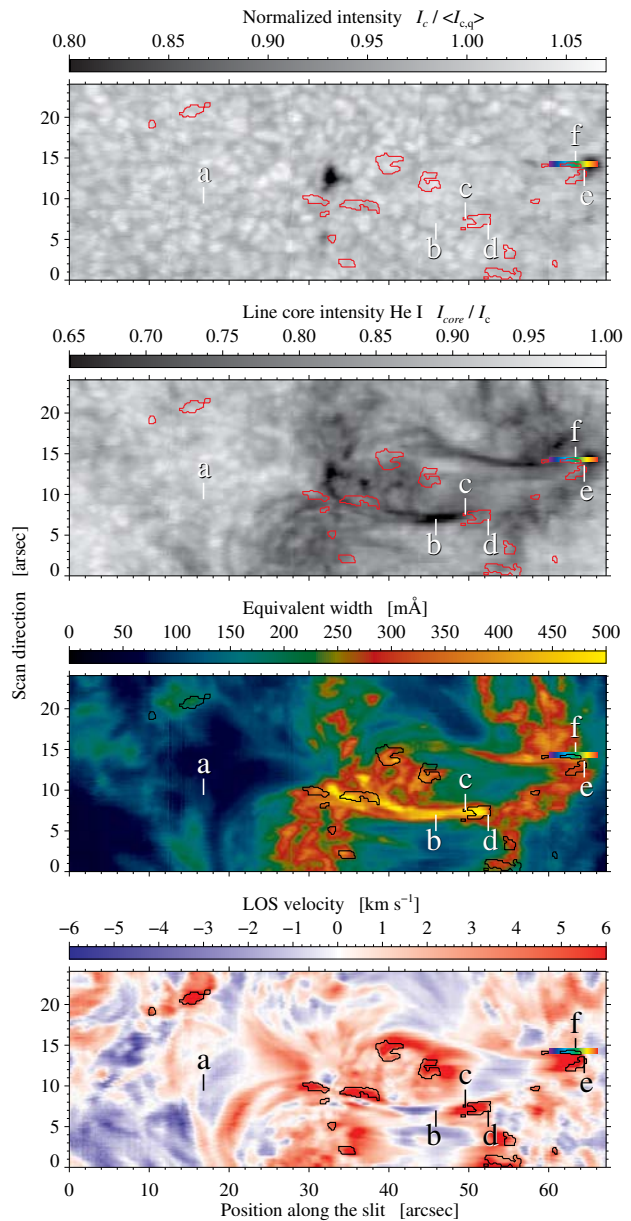
Fig. 2 GRIS slit-reconstructed images on 2015 April 17 at 08:42 UT of the observed region. From top to bottom: continuum intensity, line core intensity of the red component of the He I triplet, equivalent width, and the one-component LOS velocity. The LOS velocity was inferred using a single Lorentzian fit. The labels "a" to "f" mark the locations of six He I profiles shown in Fig. 3. The contours encompass only clearly discernible dual-flow components in He I profiles. The rainbow-colored bar in all maps marks the location of the profiles plotted in Fig. 4.

to be $I_c = 1$. Therefore, each spectrum was normalized to the local continuum before removing the telluric line.

Figure 2 shows a slit-reconstructed continuum intensity map (top) and a line-core intensity map of the red He I component (using the minimum of the line for each spectrum) normalized to the local continuum intensity I_{core}/I_{lc} (second from top).
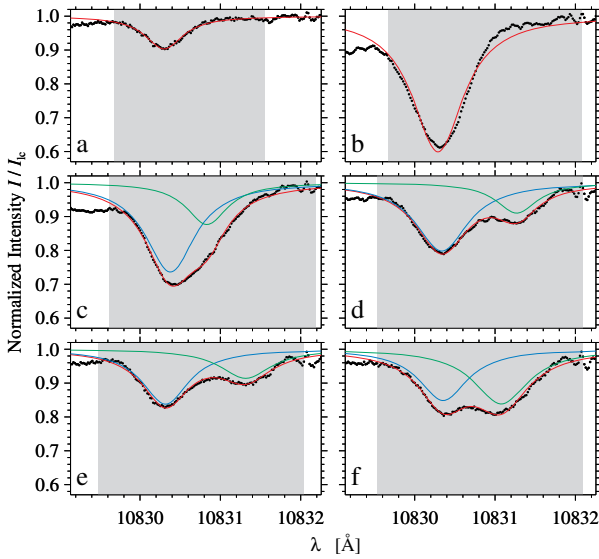
Fig. 3 The dots represent the observed He I red-component profiles and the best Lorentzian fit is shown with a solid red line. When dual-flow He I profiles are present, the fit (solid red line) is a superposition of two individual Lorentzians (blue and green solid lines). Labels "a" to "f" show the locations of the profiles in the map of Fig. 2. The grey background marks the fitting range.

3 Method

Most of the He I 10830 Å intensity profiles show the expected two spectral lines, which comprise the blue and red components. However, a few percent of these profiles, in our data set around 3 %, shows a clear signature of a fast component in the He I triplet (see the contours in Fig. 2). As a first approach we assume that all profiles have only one component. Hence, we use a single Lorentzian profile to fit all He I profiles:

$$F = 1 - \frac{A_0}{u^2 + 1} \quad \text{with} \tag{1}$$

$$u = \frac{x - A_1}{A_2}, \tag{2}$$

where A_0 is the amplitude, A_1 the peak centroid, A_2 the half-width-at-half-minimum (HWHM), and the equation is set to unity to normalize the synthetic intensity continuum. The profiles were fitted using the Levenberg-Marquardt least-squares minimization (Moré 1977; Moré & Wright 1993), where the MINPACK-1 software package was implemented in IDL by Markwardt (2009). An advantage of using this routine is that it is possible to impose an upper and lower bounding limit for each free parameter of Eq. (1) independently. As a first approach, we retrieved suitable limits by fitting the mean quiet-Sun profile. The limits were then modified to increase the accuracy of the fits. The fitted wavelength range is automatically adjusted depending on the amplitude of the spectral profile. The larger the amplitude of the line the broader the spectral range. Since the dual-flow profiles are systematically redshifted we did not include the blue component in the analysis.
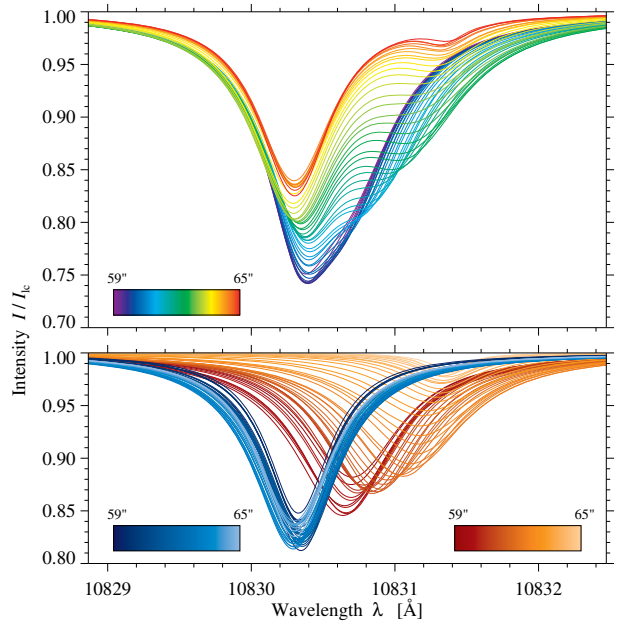
Fig. 4 *Top*: synthetic He I dual-flow profiles using the fit parameters retrieved from the double-Lorentzian fits. The color-coded bar extends over a distance of ∼ 6″ (see Fig. 2) linking profiles and positions. Note that dual-flow components are hardly discernible in the first (violet) and last (red) profiles. *Bottom*: decomposition of the dual-flow profiles into two Lorentzian (blue and red) components.

The LOS velocities inferred with the single Lorentzian fits are shown in Fig. 2 (bottom). Positive velocities are related to downflows (red) while negative velocities (blue) represent upflows. Note that double-peaked profiles, i.e., dual-flow He I profiles, are not well fitted with a single Lorentzian profile. Since the wavelength is given on an absolute scale, the wavelength reference for the LOS velocities was set to 10830.30 Å, which corresponds to the average laboratory wavelength of the He I red component (10830.25 Å and 10830.34 Å respectively, from the NIST database). Figure 2 also shows the equivalent width (second from bottom) obtained from the single-Lorentzian fits.

The next step concerns fitting the dual-flow profiles with a double-Lorentzian profile:

$$F = 1 - \frac{A_0}{u_1^2 + 1} - \frac{A_3}{u_2^2 + 1} \quad \text{with} \tag{3}$$

$$u_1 = \frac{x - A_1}{A_2} \quad \text{and} \quad u_2 = \frac{x - A_4}{A_5}, \tag{4}$$

where $A_{0,3}$ are the amplitudes, $A_{1,4}$ are the centroids, and $A_{2,5}$ are the HWHM of each Lorentzian, respectively. Due to the very short computation time (a few minutes), all spectral profiles were fitted again with two Lorentzians. However, in the future we will adapt the code to only fit the two-component profiles.

An adaptive wavelength range was not used this time. We chose two different wavelength ranges depending on the position of the line core of the He I red component. This ignored the He I blue component from the selected wavelength
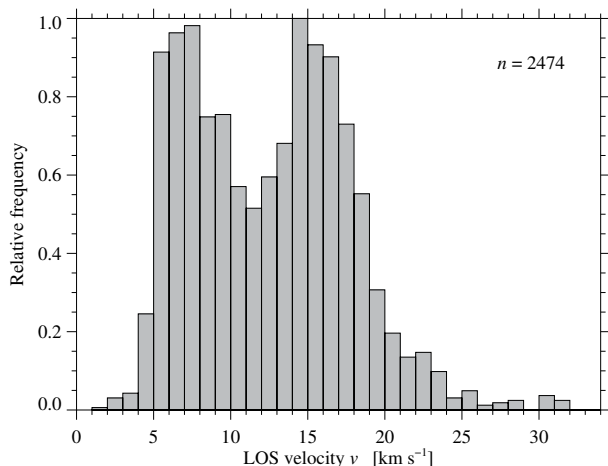
Fig. 5 Normalized frequency distribution of the LOS velocities of the redshifted He I component obtained with dual-flow fitting using two Lorentzians. The variable n is the total number of pixels which were used for the histogram. The pixels belong to the areas encompassed by the contours shown in Fig. 2.

range. Therefore, if the line core of the He I red component was located below 10830.49 Å, then the wavelength range was $[-0.83, +1.73]$ Å with respect to the line core. Otherwise, if the position of the line core was > 10830.49 Å, then the wavelength range was $[-1.37, +1.73]$ Å with respect to the line core.

The initial estimates of the fit parameters A_0–A_5 were based on the single-Lorentzian fits and on the location of the deepest line core of the dual-flow components. The peak centroid of the fast component is always more redshifted than the slow component. The peak centroid of the slow component is always at rest. The amplitudes A_0 and A_3 are both initially set to the amplitude inferred from the single-Lorentzian fit, but are allowed to vary in the course of the fitting. The parameters A_2 and A_5 have a fixed value of the HWHM of 0.32 Å (mean HWHM values of all the profiles fitted with a single Lorentzian).

In order to localize the dual-flow profiles, different types of these profiles were manually selected and then correlated with all the profiles of the map. The wavelength range for this correlation was between $[10829.50$–$10832.56]$ Å. In our particular case, we have selected more than 70 clearly distinguishable dual-flow profiles. Weak dual-flow profiles like, for instance, the first violet and red (too small amplitude) synthetic profiles shown in Fig. 4, were not selected because they are too weak to clearly identify the fast component. The median value of the correlation of all profiles were used as a threshold. Hence, only profiles which showed a larger correlation factor than 0.98% were treated as two-component profiles. The contours in Fig. 2 encompass these profiles. Developing an automatic algorithm to select the dual-flow profiles remains as future work.

4 Results

Some examples to illustrate the quality of the fitting method are shown in Fig. 3. All profiles are also marked in Fig. 2. Profile a represents a common quiet-Sun profile with a LOS velocity close to zero (-0.01 km s^{-1}). An example of a profile with a large equivalent width (472.4 mÅ) is shown in panel b. It arises from a dark filamentary structure in the chromosphere (see Fig. 2). However, the LOS velocity is rather small and only reaches -0.3 km s^{-1} (upflow). Profiles c–f represent different types of dual-flow profiles. In particular, profile c was selected because of its deep line core, i.e., higher absorption. The LOS velocity of the fast component (solid green line) was about 14.8 km s^{-1} while the slow component (solid blue line) only showed about 2.2 km s^{-1}. Profiles d and e are located near the footpoints of the filamentary structure. The latter had one of the largest inferred velocities of the fast component (~ 28.1 km s^{-1}). The remaining profile f presents two components with similar amplitudes. The fast component reached a LOS velocity of about 21.5 km s^{-1}.

The normalized frequency distribution of the LOS velocities belonging to the He I fast component is shown in Fig. 5. Velocities are in the range of 1–32 km s^{-1}. The distribution is clearly double-peaked. The maxima are located close to 7 km s^{-1} (subsonic) and 16 km s^{-1} (supersonic), respectively. However, two distinct populations cannot be identified in the FOV, either because the statistical sample is too small or sub-/supersonic flows are transitory in a confined space. Our normalized frequency distribution is similar to the one reported by Aznar Cuadrado et al. (2007) in magnetic field-free areas.

We traced the distribution of the dual-flow profiles along a given slit position. The slit position was chosen close to the footpoints of the filamentary structure and next to the pore. The rainbow-colored bar in Fig. 2 shows the location of the profiles. For an easy inspection, the colors in the color bar are associated to the colors of the 44 profiles shown in Fig. 4. We do not plot the observed profiles to avoid a crowded display. Instead, Fig. 4 shows the synthetic profiles computed from the inferred parameters of the double-Lorentzian fits. One interesting observational feature seen in the top panel of Fig. 4 is that the first profiles (violet profiles) only have the slow component. However, once we enter the area of the footpoints (turquoise-green profiles) a clearly fast component appears. The shifted profiles next to the pore exhibit the strongest redshifts (green-yellow profiles) but possess the smallest amplitudes. The bottom panel of Fig. 4 shows the individual Lorentzian profiles, which yield the dual-flow profile shown in the top panel. Blue colors always show the slow component while red colors show the fast component. The slow component is always stationary around the reference laboratory wavelength 10830.30 Å, whereas the fast component is always redshifted reaching values of up to 10831.40 Å in the line core.

Random and systematic errors can influence the measurements. Using the noise estimate ($\sigma = 3.3$ %) based on

continuum intensity variations (see Sect. 2.1) and the fit parameters from Eqs. (1) and (2) for single Lorentzian profiles, mock spectra are created and analyzed in the same way as the observed data. The linear correlation coefficient for amplitude and HWHM is $\rho = 0.99$ and that for the velocity is $\rho = 0.94$. However, higher Doppler speeds are underestimated. The 3σ-uncertainties for amplitude, velocity, and HWHM are 2.2 %, 210 m s^{-1}, and 1.17 pm, respectively, whereas the mean values and the shape of the distributions are barely affected. These random errors also apply to the double-Lorentzian fits, which are however additionally influenced by systematic errors. Dual-flow profiles imply high velocities for the fast component. Therefore, the slow component of the He I red component will be blended with the fast component of the He I blue component.

Using the fit parameters of Eqs. (3) and (4) for the red He I doublet and scaling them appropriately for the blue line of the He I triplet, mock spectra are generated to obtain an error estimate. The aforementioned blend mostly impacts the blue wing of the slow component of the He I red component, which leads on average to a -300 m s^{-1} zero point offset for the velocity and a 3σ-uncertainty of 1.24 km s^{-1}. On average the amplitude of the slow component is overestimated by 8 % with a 3σ-uncertainty of about 27 %. In principle, these systematic errors can be reduced either by fitting the entire He I triplet or by appropriately modeling the He I triplet's blue line when fitting the red doublet. In summary, random and systematic errors are sufficiently small to allow a scientific interpretation of the 2D maps of physical parameters (for example those in Fig. 2) and of dual-flow He I spectral profiles.

5 Conclusions and outlook

In this paper we introduce a simple and rapid technique for determining the velocity of multiple atmospheric components within a single spatial pixel. This technique produces good fits and gives reasonable velocity values, suggesting that after some further tests it can be applied to additional data. For example, an implicit assumption is that the He I line is always optically thin in the wavelength range of the telluric line and has to be tested.

We presented GRIS observations of an EFR containing two small pores. The observations were complemented with simultaneous imaging spectropolarimetry acquired with the GFPI in the photospheric Fe I 6302 Å line. The FOV for the broad-band images is shown in Fig. 1 (red box). In addition, simultaneous observations with CRISP were carried out. Several full spectropolarimetric scans of the photospheric Fe I 6173 Å line and the chromospheric Ca II 8542 Å line were taken with a FOV of 54″×54″ (blue box in Fig. 1).

The remaining task will be to extract all the information of the available data sets to understand the physical processes that lead to the formation, evolution, and disappearance of these filamentary structures. The photospheric Fe I 6302 Å and 6173 Å lines from GFPI and CRISP will

be used to study the dynamics and temporal evolution of photospheric structures. In addition, the former data will be complemented by the photospheric lines acquired with GRIS, e.g., Si I 10827 Å, Ca I 10834 Å, and Ca I 10839 Å, in order to track the dynamics along several heights within the photosphere. The dynamics in the chromosphere will be covered by the He I 10830 Å triplet as well as with the Ca II 8542 Å line. By analyzing all available GRIS scans we will be able to further characterize the dual-flow profiles seen in the He I triplet and thus elucidate the origin of the two populations shown in Fig. 5.

The link between the chromospheric filamentary structures and the underlying photosphere is still an open question. Does the plasma of the chromospheric structures, which exhibit supersonic LOS downflows near the footpoints, reach the photosphere? Are the loops also seen in the corona and if yes, what is their behavior? SDO can provide such information (e.g., in the quiet corona and upper transition region with Fe IX 171 Å EUV images) to study the evolution of the loops in the corona. The magnetic field information of the photosphere and the chromosphere will be obtained based on high-resolution imaging spectropolarimetric data observed with CRISP.

Regarding the method to fit the dual flows, we need to expand our study to different data sets. The goal is to build a database, which includes many different types of He I 10830 Å profiles to automatically detect the ones with dual-flow components. This database will include profiles extracted from (more mature) active regions, sunspots, arch filament systems, and quiet-Sun regions. The χ^2-statistics of the fit can provide hints, where a single component fit is not sufficient. However, noise and the strength of the He I absorption feature potentially obfuscate such a simplistic approach. Therefore, an automatic detection of dual-flow profiles has to rely on easily measured line properties as, for example, the line asymmetry. Additional improvements of the algorithm concern the blue component of the He I triplet. In double-peaked profiles, the fast blue component blends with the slow red component, thus affecting the accuracy of the double-Lorentzian fitting method.

References

Allende Prieto, C., Asplund, M., & Fabiani Bendicho, P. 2004, A&A, 423, 1109

Asensio Ramos, A., Trujillo Bueno, J., & Landi Degl'Innocenti, E. 2008, ApJ, 683, 542

Avrett, E. H., Fontenla, J. M., & Loeser, R. 1994, in Infrared Solar Physics, eds. D. M. Rabin, J. T. Jefferies, & C. Lindsey, IAU Symp., Vol. 154, 35

Aznar Cuadrado, R., Solanki, S. K., & Lagg, A. 2005, in Chromospheric and Coronal Magnetic Fields, eds. D. E. Innes, A. Lagg, & S. A. Solanki, ESA Special Publ., Vol. 596, 49.1

Aznar Cuadrado, R., Solanki, S. K., & Lagg, A. 2007, in Modern Solar Facilities – Advanced Solar Science, eds. F. Kneer, K. G. Puschmann, & A. D. Wittmann, p. 173

Berkefeld , T., Schmidt, D., Soltau, D., von der Lühe, O., & Heidecke, F. 2012, AN, 333, 863

Collados, M., López, R., Páez, E., et al. 2012, AN, 333, 872

Denker, C., Balthasar, H., Hofmann, A., Bello González, N., & Volkmer, R. 2010, in Ground-Based and Airborne Instrumentation for Astronomy III, eds. I. S. McLean, S. K. Ramsay, & H. Takami, Proc. SPIE, Vol. 7735, 77356M

Denker, C., von der Lühe, O., Feller, A., et al. 2012, AN, 333, 810

Kuckein, C., Martínez Pillet, V., & Centeno, R. 2012, A&A, 542, A112

Lagg, A., Ishikawa, R., Merenda, L., et al. 2009, in The Second Hinode Science Meeting: Beyond Discovery-Toward Understanding, ed. B. Lites, M. Cheung, T. Magara, J. Mariska, & K. Reeves, ASP Conf. Ser., Vol. 415, 327

Lagg, A., Woch, J., Krupp, N., & Solanki, S. K. 2004, A&A, 414, 1109

Lagg, A., Woch, J., Solanki, S. K., & Krupp, N. 2007, A&A, 462, 1147

Markwardt, C. B. 2009, in Astronomical Data Analysis Software and Systems XVIII, eds. D. A. Bohlender, D. Durand, & P. Dowler, ASP Conf. Ser., Vol. 411, 251

Moré, J. J. 1977, in Numerical Analysis,, ed. G. A. Watson, Lect. Notes in Math., Vol. 630, 105

Moré, J. J. & Wright, S. J. 1993, Optimization Software Guide, (Philadelphia: Society for Industrial and Applied Mathematics (SIAM)), Front. Appl. Math., Vol. 14

Muglach, K., Schmidt, W., & Knoelker, M. 1997, Sol. Phys., 172, 103

Muglach, K. & Sütterlin, P. 1998, in Three-Dimensional Structure of Solar Active Regions, eds. C. E. Alissandrakis & B. Schmieder, ASP Conf. Ser., Vol. 155, 341

Neckel, H., & Labs, D. 1984, Sol. Phys.,, 90, 205

Penn, M. J., & Kuhn, J. R. 1995, ApJ, 441, L51

Pesnell, W. D., Thompson, B. J., & Chamberlin, P. C. 2012, Sol. Phys., 275, 3

Puschmann, K. G., Denker, C., Kneer, F., et al. 2012, AN, 333, 880

Sasso, C., Lagg, A., & Solanki, S. K. 2011, A&A, 526, A42

Sasso, C., Lagg, A., Solanki, S. K., Aznar Cuadrado, R., & Collados, M. 2007, in The Physics of Chromospheric Plasmas, eds. P. Heinzel, I. Dorotovič, & R. J. Rutten, ASP Conf. Ser., Vol. 368, 467

Scharmer, G. B., Bjelksjo, K., Korhonen, T. K., Lindberg, B., & Petterson, B. 2003, in Innovative Telescopes and Instrumentation for Solar Astrophysics, eds. S. L. Keil & S. V. Avakyan, SPIE Conf. Ser., Vol. 4853, 341

Scharmer, G. B., Narayan, G., Hillberg, T., et al. 2008, ApJ, 689, L69

Scherrer, P. H., Schou, J., Bush, R. I., et al. 2012, Sol. Phys., 275, 207

Schmidt, W., Muglach, K., & Knölker, M. 2000, ApJ, 544, 567

Schmidt, W., von der Lühe, O., Volkmer, R., et al. 2012, AN, 333, 796

Schou, J., Scherrer, P. H., Bush, R. I., et al. 2012, Sol. Phys., 275, 229

Socas-Navarro, H. 2001, in Advanced Solar Polarimetry – Theory, Observation, and Instrumentation, eds. M. Sigwarth, ASP Conf. Ser., Vol. 236, 487

Teriaca, L., Falchi, A., Cauzzi, G., et al. 2003, ApJ, 588, 596

Volkmer, R., Eisenträger, P., Emde, P., et al. 2012, AN, 333, 816